

Determination of isotropic elastic constants from dispersion images based on ultrasonic guided waves by using neural networks

Mathias Held^{*}, Jannis Bulling, Yevgeniya Lugovtsova, Jens Prager

Bundesanstalt für Materialforschung und -prüfung, Unter den Eichen 87, Berlin 12205, Germany



ARTICLE INFO

Keywords:
Ultrasonic guided waves
Dispersion
Elastic constants
Neural networks
Image processing
Vision Transformer

ABSTRACT

This article presents a method to use the dispersive behavior of ultrasonic guided waves and neural networks to determine the isotropic elastic constants of plate-like structures through dispersion images. Therefore, two different architectures are compared: one using convolutions and transfer learning based on the EfficientNetB7 and a Vision Transformer-like approach. To accomplish this, simulated and measured dispersion images are generated, where the first is applied to design, train, and validate and the second to test the neural networks. During the training of the neural networks, distinct data augmentation layers are employed to introduce artifacts appearing in measurement data into the simulated data. The neural networks can extrapolate from simulated to measured data using these layers. The trained neural networks are assessed using dispersion images from seven known material samples. Multiple variations of the measured dispersion images are tested to guarantee the prediction stability. The study demonstrates that neural networks can learn to predict the isotropic elastic constants from measured dispersion images using only simulated dispersion images for training and validation without needing an initial guess or manual feature extraction, independent of the measurement setup. Furthermore, the suitability of the different architectures for generating information from dispersion images in general and an image-to-regression visualisation technique, are discussed.

1. Introduction

The exact determination of elastic material properties is fundamental in many engineering fields. It is necessary not only for designing components to meet safety and lifetime requirements but also for numerical modeling of components or structures. Furthermore, this knowledge can help choose optimized parameters, e.g., for milling or forming while processing raw materials or evaluating and understanding degradation processes within materials or components. Overall, detailed knowledge about the material properties can increase safety, help conserve resources, reduce energy consumption, and thus contribute to environmental sustainability and cost efficiency.

However, the information on material parameters provided by manufacturers, especially for polymers and fiber-reinforced plastics, often seems insufficient as it depends on the production process parameters. In practical applications, polymer materials, fiber-reinforced plastics, and metals frequently occur as plate-like structures where ultrasonic guided waves (UGWs) can propagate.

This article proposes using neural networks to determine the elastic

constants from dispersion images of UGW propagation in the wavenumber-frequency domain. UGWs and dispersion images have the advantage that the data obtained represents an average of the material properties over the measured range. Additionally, UGWs can be measured in situ, and the measurement process is non-destructive. Once the neural networks are trained, their independence from any initial guess or manual feature extraction enables straightforwardly automating the entire material characterization process. The presented neural models are independent of the measurement setup. Instead of attempting to replicate artifacts from a specific measurement setup, only perfect numerical data, including randomly added artifacts, are used for training. Therefore, the presented approach requires minimal prior knowledge of the material and measurement system.

The basis of all inverse methods for determining elastic constants from wave propagation is the assumption that they are sensitive to changes in material properties and can be uniquely assigned to a material state. According to [1], at least three different modes are required to determine the elastic constants of an anisotropic composite material based on group velocities for a unique determination [2]. conducted a

* Corresponding author.

E-mail address: Mathias.Held@bam.de (M. Held).

sensitivity analysis on dispersion images to evaluate the impact of isotropic elastic constants on the modes. The study found that changes in the elastic modulus had a more significant effect on higher frequency modes. However, determining the sensitivity of different modes to Poisson's ratio was challenging due to significant variation over the frequency-wavenumber range. The study recommends using the S1 mode to determine Poisson's ratio due to the low sensitivity of the fundamental modes A0 and S0 in isotropic materials. The sensitivity to elastic constants varies in the case of transversely isotropic materials. Some modes, or specific regions within a mode in the wavenumber frequency spectrum, are sensitive to changes in material parameters, while other regions are not. For comprehensive characterization of all parameters, it is advisable to use a broadband signal that includes higher order modes, as this approach ensures coverage of the sensitive areas within the modes.

This work assumes that neural networks can link mode information from different frequency-wavenumber ranges in dispersion images to determine material parameters clearly and precisely. It is postulated that even single modes with low sensitivity to material parameters can be valuable when combined with other information in the dispersion images since a neural network could evaluate complex patterns by combining information from different modes.

Besides employing dispersion images from UGWs combined with machine learning algorithms, conventional non-destructive methods for determining elastic constants are already described in the literature. The authors [3] use ultrasonic longitudinal wave speed data to determine the elastic constants of an anisotropic solid, while [4] already utilized the pulse-echo method to determine the elastic constants of a single-crystal material. The use of the pulse transmission method to determine the elastic constants of fiber composites is presented in [5,6] infer elastic and viscoelastic properties of thin anisotropic plates through inversion of the spectrum of the transmitted plane waves. The authors [7] use the ultrasonic polar scan technique to determine the local elastic constant of a thin orthotropic material.

Many researchers use conventional mathematical methods to evaluate the dispersion relation of UGW to determine the elastic constants. The researchers in [8] and [9] describe the use of dispersion images in the wavenumber-frequency domain for determining the elastic constants of isotropic materials by using the point of zero group velocity. The authors [10] compare different reconstruction methods based only on wavelength and group velocity of A0 and S0 mode to determine the elastic properties of a layered structure, and [11] study the inverse problem for determining orthotropic material properties from dispersion images in the frequency-wavenumber domain. Similarly, [12] use an optimization approach to determine the material properties of fiber-reinforced composites. There, a genetic algorithm is employed to minimize the difference between dispersion curves in the frequency-wavenumber domain calculated numerically and those obtained experimentally for multiple directions. A similar approach is published in [13], where the authors determine elastic constants based on dispersion images in the time-frequency domain. Besides determining the elastic constants, some researchers, e.g., [14] or [15], also determine damping by introducing attenuation coefficients.

In addition to these approaches, which use mainly conventional mathematical methods, a few researchers use neural networks to determine elastic material parameters from UGWs dispersion relation. Authors [16] use a simple, fully connected (dense) neural network to predict all nine elastic constants of an orthotropic material. Therefore, the matrix pencil decomposition method extracts the wavenumber and frequency values of the different propagating wave modes from a dispersion image in the wavenumber/frequency domain created from space/time measurement data. The extracted wavenumber and frequency values are then used as input for the network. The authors [17] propose a recurrent neural network using a time-frequency vector of UGW propagation as input to predict the elastic constants. Other authors [18] use a supervised regression-based 1D convolutional neural network

(CNN). Their 1D CNN uses the A0 and S0 modes time series measured from UGW propagation as input to predict elastic constants.

Furthermore, 2D CNN architectures for image recognition tasks are already well known [19] and are still being further developed. A 2D CNN with polar group velocity representation from UGW as input is used to characterize materials and predict the elastic constants [20]. The study [21] introduces a 2D CNN utilising stacked time-series data from UGW propagation. The objective is to estimate static and dynamic loads. They use the LeNet-5 [22] architecture as the baseline architecture for their 2D CNN and thus employ transfer learning. While 2D CNNs were initially designed for classification tasks, the authors [20,21] modified their architecture to extract wave propagation features from the input to solve a regression task.

Physics-informed neural networks (PINN) are promising for making credible predictions, with strong generalization and extrapolation capabilities, even when the training-data availability is limited. However, their effectiveness is contingent upon the precision of the embedded physical laws and the problem's complexity. When exploring novel correlations within the data or when the underlying formula lacks precision, conventional neural networks using standard optimizers, which are not constrained by a predefined optimization-search-space, may offer superior performance. PINNs remain relatively underexplored within the presented context [23] used PINNs to quantify surface-breaking cracks in an aluminum plate by predicting the velocity of an ultrasonic wave. Their model is Physics-informed because the loss function used to train the model is based on the acoustic wave equation. In [24], a comparable physical-informed method is used to determine, among other things, the elastic constants of a polycrystalline Nickel plate. The presented model utilises displacement in time and space as input data and employs an optimizer based on a loss function derived from the acoustic wave equation. Considering the availability of sufficient simulated training data and the necessity of a specialized architecture for a PINN in order to accommodate dispersion relations, as well as the requirement for dispersion images to be simulated for each output during the training process, which would result in a significant increase in the time required for the training process, it can be concluded that these networks are beyond the scope of this study.

In summary, dispersion images from UGW propagation are commonly employed by researchers, particularly in the frequency-wavenumber format, to calculate the elastic constants by conventional mathematical methods. Recently, neural networks (NNs) have gained importance for estimating elastic constants from dispersion relations.

This article combines both by using well-known dispersion images in the wavenumber-frequency domain and treating it as an image processing problem, as done for other image-like UGW representations, to solve the problem of determining the isotropic elastic constants. Converting the problem to the wavenumber-frequency domain and consequently to the field of image processing holds the advantage that the data is already well-filtered by the 2D FFT. Furthermore, this enables the use of various image augmentation techniques to generate more diverse training data and facilitate straightforward optical verification of the data and results. Furthermore, the multi-modal information can be used without identifying and separating the different propagating, potentially crossing, or untraceable wave modes.

The selection of NNs for determining isotropic elastic constants from dispersion images is driven by several key factors. Traditional methods often require manual feature extraction and initial parameter guesses, which can be time-consuming and prone to human error. In contrast, neural networks, particularly CNNs and Vision Transformers, offer significant advantages in automation and accuracy by directly processing dispersion images without the need for manual intervention. One of the primary reasons for selecting NNs is its ability to handle complex patterns in dispersion images through advanced image processing capabilities. The neural networks are trained to recognise intricate relationships between wave propagation modes and material properties, enabling precise prediction of elastic constants from the dispersion data.

This capability is particularly valuable when dealing with materials that exhibit minor changes in properties, which might be challenging to detect using conventional techniques.

Furthermore, the method's robustness across different conditions enhances its practical applicability. The use of simulated data for training, including various data augmentation techniques to cover real-world artefacts, ensures that the neural networks can generalise well to real-world measurements, even when those measurements contain various artefacts and noise. This is crucial for in-situ and non-destructive testing applications, where consistent and reliable results are needed despite variations in the measurement environment. The presented EfficientNetB7-like CNN architecture uses pre-trained layers and weights from ImageNet as start values, an approach known as transfer learning. The second architecture is a Vision Transformer-like architecture that uses random start values within the layers. Both architectures have been adapted from solving classification tasks to the presented regression problem of predicting elastic constants. A Hyperparameter search is done to identify a well-suited architecture and parameters. Both models are compared regarding their performance, robustness, and suitability for solving the presented problem and handling graph-like data in general. The presented neural networks have been trained using only simulated dispersion images comprising a wide range of isotropic elastic constants. The created models were tested on seven different measured material samples to ensure reliable predictions for measurement data across the entire value range. The selected value range comprises common metals and polymers.

This approach represents a novel methodology, employing neural networks from the field of image processing to determine elastic constants directly from dispersion images in the wavenumber-frequency domain. In conclusion, the proposed approach utilising NNs for determining isotropic elastic constants is selected for its capacity to automate the characterisation process, accommodate complex and noisy data, and provide reliable predictions across diverse conditions. This renders it

particularly valuable in real-time industrial applications, such as quality assurance of materials and structural health monitoring, where speed, accuracy, and robustness are paramount. Additionally, an adapted attention-mapping technique is presented to visualise the prediction of an image-to-regression problem.

2. Datasets and modelling

An outline of the development process described in this article is shown in Fig. 1. The initial stages include data acquisition, transformation, and preprocessing. Subsequently, a model and its related parameters are chosen. Finally, the chosen model is explained and evaluated. This structure follows the suggested procedure outlined in [25] pp.41 and pp.77ff.

2.1. Isotropic elastic constants

In general, many metals and polymers can be assumed to be macroscopically isotropic. The isotropic elastic constants describe a material with non-directional linear elastic properties. Young's modulus (E) and Poisson's ratio (ν) are two elastic constants that define the complete isotropic stiffness matrix in Voigt notation. The resulting compliance matrix is the inverse of the stiffness matrix, as shown in Eq. (1). In addition, the density (ρ) and the thickness are the parameters that influence the shape of the curves in dispersion images.

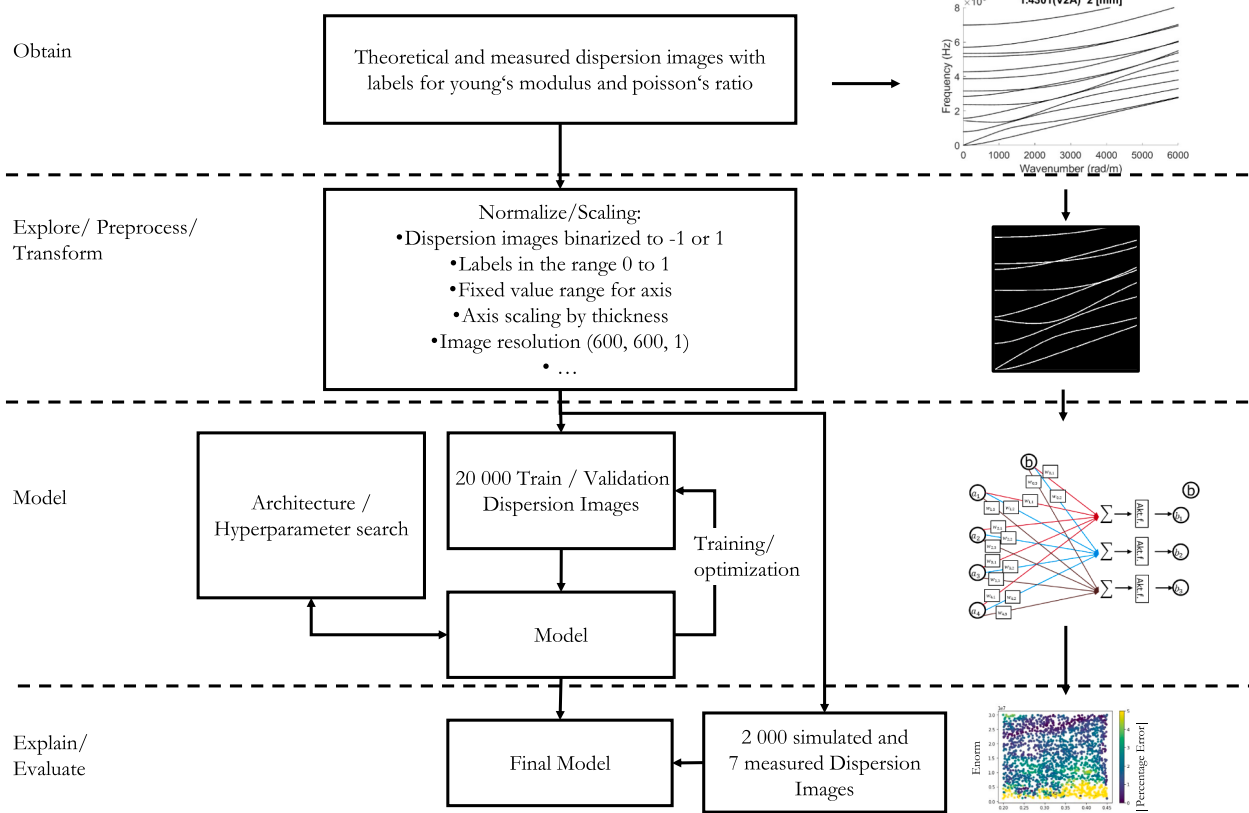


Fig. 1. Overview of the data flow.

$$C^{-1} = \begin{bmatrix} \frac{1}{E} & -\frac{\nu}{E} & -\frac{\nu}{E} & 0 & 0 & 0 \\ -\frac{\nu}{E} & \frac{1}{E} & -\frac{\nu}{E} & 0 & 0 & 0 \\ -\frac{\nu}{E} & -\frac{\nu}{E} & \frac{1}{E} & 0 & 0 & 0 \\ 0 & 0 & 0 & \frac{2*(1+\nu)}{E} & 0 & 0 \\ 0 & 0 & 0 & 0 & \frac{2*(1+\nu)}{E} & 0 \\ 0 & 0 & 0 & 0 & 0 & \frac{2*(1+\nu)}{E} \end{bmatrix} \quad (1)$$

2.2. Simulated dataset

A labeled dataset is necessary to train a neural network using a supervised learning approach. The Scaled Boundary Finite Element Method (SBFEM) [26,27] is a semi-analytical numerical simulation technique to simulate the dispersion images for structures with given elastic constants. The simulated dispersion images are generated by solving the eigenvalue problem of the SBFEM Eq. (2) for specific wavenumbers, which provides the corresponding frequency values. The simulated isotropic elastic constants are uniformly distributed within the dataset to prevent the NNs from focusing on an over-represented range of elastic constants. A total of 20,000 dispersion images is generated to cover the specified value range, given in Table 1. An additional randomly distributed dataset containing 2000 dispersion images is generated for testing. The large simulated data set allows the NNs to learn a wide range of materials within the selected range of values, including common metals, polymers, and even non-existent materials.

The trajectory of the modes of the UGWs within a dispersion image in the frequency-wavenumber domain is directly proportional to the thickness of the plate. To simplify the simulation process, we can normalize the axis by thickness as done in previous studies, e.g. [8,9]. This method facilitates comparison across different thicknesses, enhancing the robustness of the material characterization. The x-axis results in wavenumber \times thickness and the y-axis in frequency \times thickness. Instead of using Young's modulus and density directly, two normalized quantities are applied, $E_{norm} = E/\rho$, and $\rho_{norm} = 1$. Since ρ_{norm} and the thickness is set to one, E_{norm} and Poisson's ratio (ν) are the only parameters to be defined for calculating the shape of the curves. Hence, these two parameters can be learned from the dataset and thus predicted by the models.

The simulation of one image takes approximately two seconds on an up-to-date desktop PC. The resulting dispersion images contain clear point/pixel-wise information without artifacts and noise, as shown in Fig. 2 (Input).

2.3. Measurement dataset

The measurement data was recorded using a Verasonics Vantage 64 with a sampling frequency of 62.5 MHz. A phased array system (Olympus 2.25-L-64-48X12-A2-P-2.5-HY) 64 Elements, with an average center frequency of ~ 2.41 MHz and a pitch of 0.75 mm, is used. The first element of the array is used to excite the UGW and the other 63 elements are used for recording. The resolution in the wavenumber \times

Table 1

Value range of the isotropic elastic constants for simulating the dispersion images. $E_{norm} = E/\rho$, Young's modulus proportional to the density of the material.

		E_{norm} [m ² /s ²]	Poisson's ratio (ν)
Value range for the simulation	Min	1E+06	0.2
	Max	30E+06	0.45

thickness axis is limited due to the small number of elements, the minimal distance between them, and the axis scaling with thickness applied to the dispersion images. The thickness is measured at every corner of the 300 \times 300 mm plate using a micrometer screw gauge and averaged. The resulting thickness, the size, and the weight of the specimen are used to calculate the density.

We mainly implemented the procedures outlined in [28] to process the data and generate dispersion images. First, a tukey window function ($\alpha = 0.3$) is applied to the measured data in time and space dimensions. Second, the data is zero-padded to create an array having the next larger power of two as the size in each direction but at least 2^{13} entries. The 2D FFT is applied, the values are shifted to have the zero frequency at the center, and the absolute values are taken. The quarter with the desired range for frequency and wavenumber, including wave modes with a positive group velocity, is taken. Afterward, a gamma correction (compression) ($\gamma = 0.1$, gain = 1) followed by a gamma expansion ($\gamma = 3.5$, gain = 1) is applied, and the values are normalized to one. Next, the image is filtered 21 times using a blur filter (size = 3 \times 3) to smooth the gradients within the pixels, and then the adaptive threshold function from opencv2 (adaptive.Thresh_Mean_c, thresh_binary, size = 55, offset = -3) is applied. Afterward, the image is eroded (size = 3 \times 3) three times to delete noise and minor artifacts, followed by dilation (size = 3 \times 3) three times to resize the left-over areas. Finally, the image is resized, using the inter_area function, to a 600 \times 600 binary array.

Employing such an automated approach for binarizing all measured dispersion images is a trade-off between removing information and introducing or not removing noise and artifacts from the data. In total, seven different specimens are used to validate the ability of the network to generalize on various materials. The elastic constants of the different samples are shown in Table 2. The isotropic elastic constants for the measured specimens are determined using the inverse procedure described in [28] and [12]. The assumed reliability of the determined values is shown in Table 4, column label quality.

2.4. Dataset preparation

The approach presented in this article concentrates on the dispersive and multi-modal behavior of UGWs, captured and represented through dispersion images in the wavenumber-frequency domain. The dispersion images are constructed following the defined procedure to ensure coherence between different datasets from different sources.

The axes are scaled with thickness. The pixel values in the dispersion images are transformed into binary values of minus one or one since the amplitude of the modes within the dispersion images depends mainly on an unknown excitation of the waves. Both axis minimum and maximum values are adjusted to the same limits across all images. This process ensures a consistent relationship between the image boundaries and the path of the modes, establishing a uniform reference system throughout the different datasets. The range of the frequency \times thickness at the y-axis is set from 0 to 8000 [Hz \times m], and the wavenumber \times thickness at the x-axis from 0 to 6 [rad \times m/m]. As the axes scale with the specimen's individual thickness. The associated frequency and wavenumber range change accordingly within the range. The associated frequency and wavenumber range will be left blank if there is insufficient information. For example, in the case of a titanium sheet, refer to Fig. 8.

The size of the dispersion images is adjusted to (600, 600, 1) (height, width, and channels) to ensure sufficient information about the shape of the modes. The usual input size of the most well-known architectures for image classification is often smaller. However, it is known that large input sizes can provide more detailed and accurate information [29]. Furthermore, the labels, E_{norm} and Poisson's ratio (ν) are normalized between 0 and 1 using the min–max-normalization to stabilize the learning process, exemplarily shown in Eq. (2) for $E_{minmaxnorm}$ and transferable to $\nu_{minmaxnorm}$.

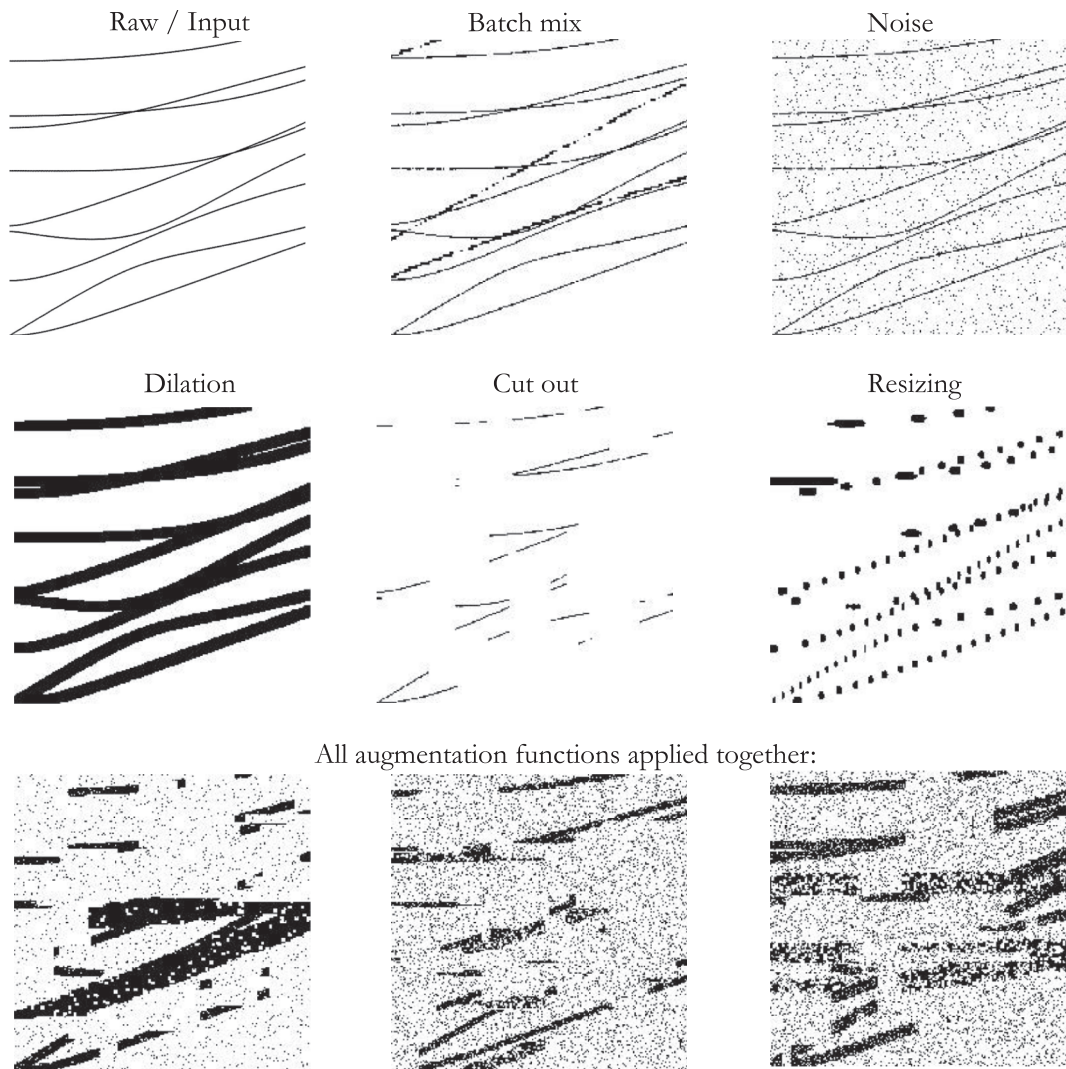


Fig. 2. From un-processed input at the top-left, through the different data augmentation functions, to the last line showing the overall effect.

Table 2

Assumed elastic constants for measured material samples. E_{norm} is Young's modulus proportional to the density of the specimen.

	Young's modulus [N/mm ²]	Density [kg/m ³]	E_{norm} [m ² /s ²]	Poisson's ratio (ν)
Aluminium castAlMg4.5Mn	7.25E+10	2657.66	2.73E+07	3.38E-01
AluminiumAl99.5	7.08E+10	2700.92	2.62E+07	3.33E-01
Stainless steel1.4016	2.04E+11	7895.33	2.58E+07	2.67E-01
Stainless steel1.4301	2.11E+11	7695.67	2.74E+07	2.85E-01
Copper sheetCW008A	1.26E+11	8952.52	1.41E+07	3.48E-01
Brass sheetCuZn CW508L	1.09E+11	8444.59	1.29E+07	3.45E-01
Titanium sheetTi2 3.7035	1.16E + 11	4506.4294	2.57E+07	3.28E-01

$$E_{min\ max\ norm} = \frac{E_{norm} - \min(E_{norm})}{(\max(E_{norm}) - \min(E_{norm}))} \quad (2)$$

2.5. Data augmentation and training

The CNN is created, trained, and evaluated using Tensorflow-2.9.1, Tensor-flow-addons-0.13.0, Keras-cv-0.3.4, and Keras-tuner-1.3.0

libraries. If not specified, the standard values of the mentioned Python 3.9.15 libraries are used.

The training dataset is split into 70 percent training and 30 percent validation data. The chosen batch size is eight for the EfficientNetB7 and 64 for the VisionTransformer architecture. Choosing the batch size is a trade-off between fast training with more generalized gradients and avoiding a memory overflow due to limited resources. The simulated training data is saved in TFRecord TensorFlow file format, and TensorFlow's Mirrored Strategy is applied to split the batch between multiple GPUs to speed up the training process. The mean-absolute-error (MAE) loss function is used with the Adam algorithm as an optimizer. Although the Adam optimizer adjusts the learning rate adaptively, the Tensorflow-Keras ReduceLROnPlateau function decreases the initial learning rate if the validation mean-squared-error difference between two consecutive epochs is less than 1e-06 for a minimum of two epochs. The training can have a maximum of 50 epochs, and the validation error is calculated at the end of every epoch. Early stopping is applied if the validation mean-squared error is not improving for longer than five epochs.

Augmentation layers within the model are employed to improve the accuracy of neural networks in predicting real-world measurement data while being only trained on simulated data. These layers offer the advantage of randomly applying augmentations to each trained image, ensuring unique inputs even within the batch while the same dataset is repeated every epoch. However, it is important to note that if new

artefacts or significantly different dispersion images appear that are not included or covered by the training data or augmentations, the prediction is likely to be broken. The implementation as a layer requires the augmentation methods to be written in TensorFlow syntax, which enables faster processing using GPU computing.

The effect of the different augmentation techniques is illustrated in Fig. 2. First, the raw input is presented, followed by the demonstration of the impact of “Batch mix”, which randomly adds parts of images within the same batch to the actual input image. This process adds realistic-looking false information to the input so that the network learns to ignore possible false information in the measurement data, e.g., due to noise or leakage effect. Adding noise makes the neural network robust to imperfections. For this purpose, two masks were created, each containing uniformly distributed random values between 0 and 1. A randomized dilation function introduces data imprecision, mimicking varying curve widths in the measurement data. The cut-out function mimics deleted information, often occurring during the preprocessing of measurement data due to low amplitudes, inappropriate threshold values, or unexcited frequencies. Since various measurement systems may provide varying amounts of data across different dimensions, the dispersion image might be resized to fit into the desired value range. A resizing layer is implemented, first downsizing followed by an upsizing, to replicate any artifacts that may arise during this interpolation procedure.

2.6. Architecture and hyperparameter search

Two different types of architectures are investigated. As the baseline architecture for building a 2D-CNN, the EfficientNetB7 architecture Tan and Quoc [29] is used. EfficientNet is one of the state-of-the-art image classification CNN architectures available within the TensorFlow-Keras library, including already pretrained weights to take advantage of transfer learning. A standard Vision Transformer architecture for classification [30] is used as a second option. Both architectures were state-of-the-art for image classification at the time of their release. The Vision Transformer-like models have a slight advantage in the famous “ImageNet” classification challenge [31]. However, there are also exceptional cases where EfficientNet-like architectures perform better, e.g. [32] if only little data is available.

In this article, both types of architecture have been adapted from classification tasks to a multi-output regression problem to solve the new task. Therefore, using the Keras-tuner and the Hyperband search function, a hyperparameter search is done to find suitable parameters for the presented regression problem. The search is limited till the tenth training epoch. The investigated search space and their results are shown in Figs. 3 and 4. The left area in each figure shows the optimized architecture, whereas the right area shows the investigated parameter space. The EfficientNetB7 architecture includes a dropout layer applied to the Global-Average-Pooling layer, which is unusual and leads to missing extracted features in the final feature map while training. Furthermore, the preprocessing layers (rescaling, layer normalization, and again rescaling) included in all EfficientNet models available at the TensorFlow-keras library are deleted. The search results may not necessarily represent the best performing model in the search space, but rather the ones that converged the fastest. This is due to the chosen algorithm, which does not train all models to the end.

The results may vary slightly upon reproduction of the process due

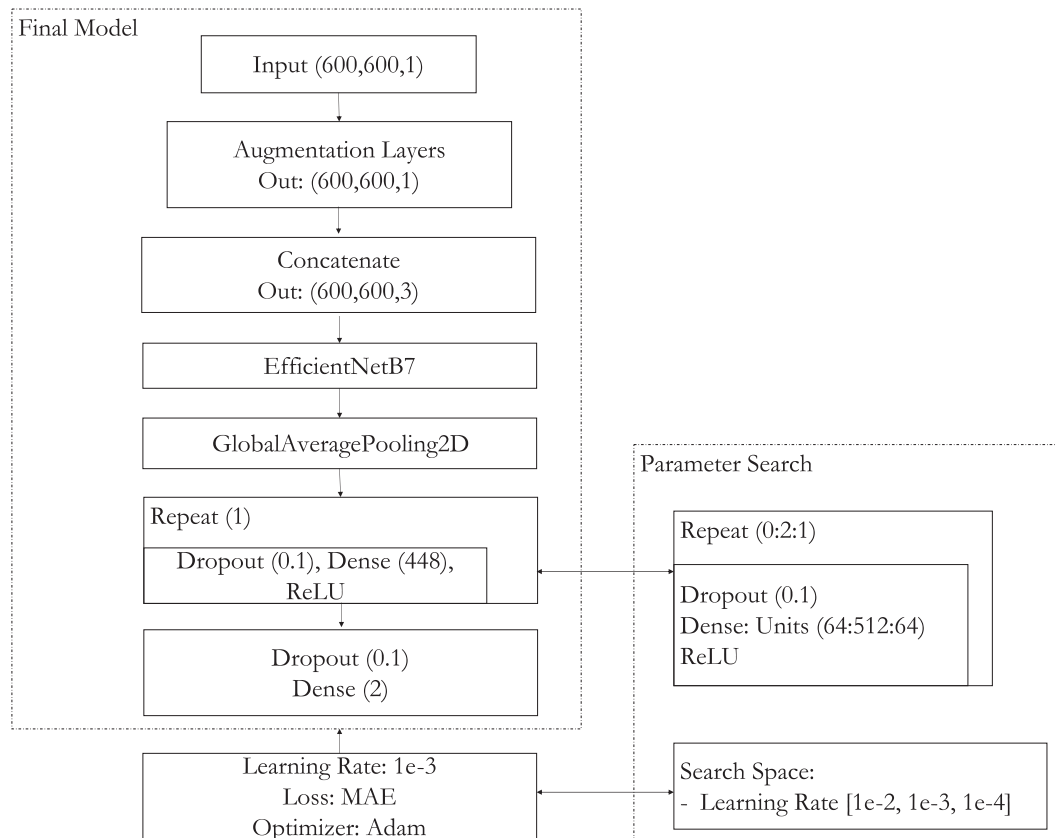


Fig. 3. The optimised architecture of the EfficientNetB7-based model and chosen hyperparameters are on the left, and the searched hyperparameters are on the right. The syntax (Start:Stop:Stepsize) and [Option 1, Option 2, ...] is used.

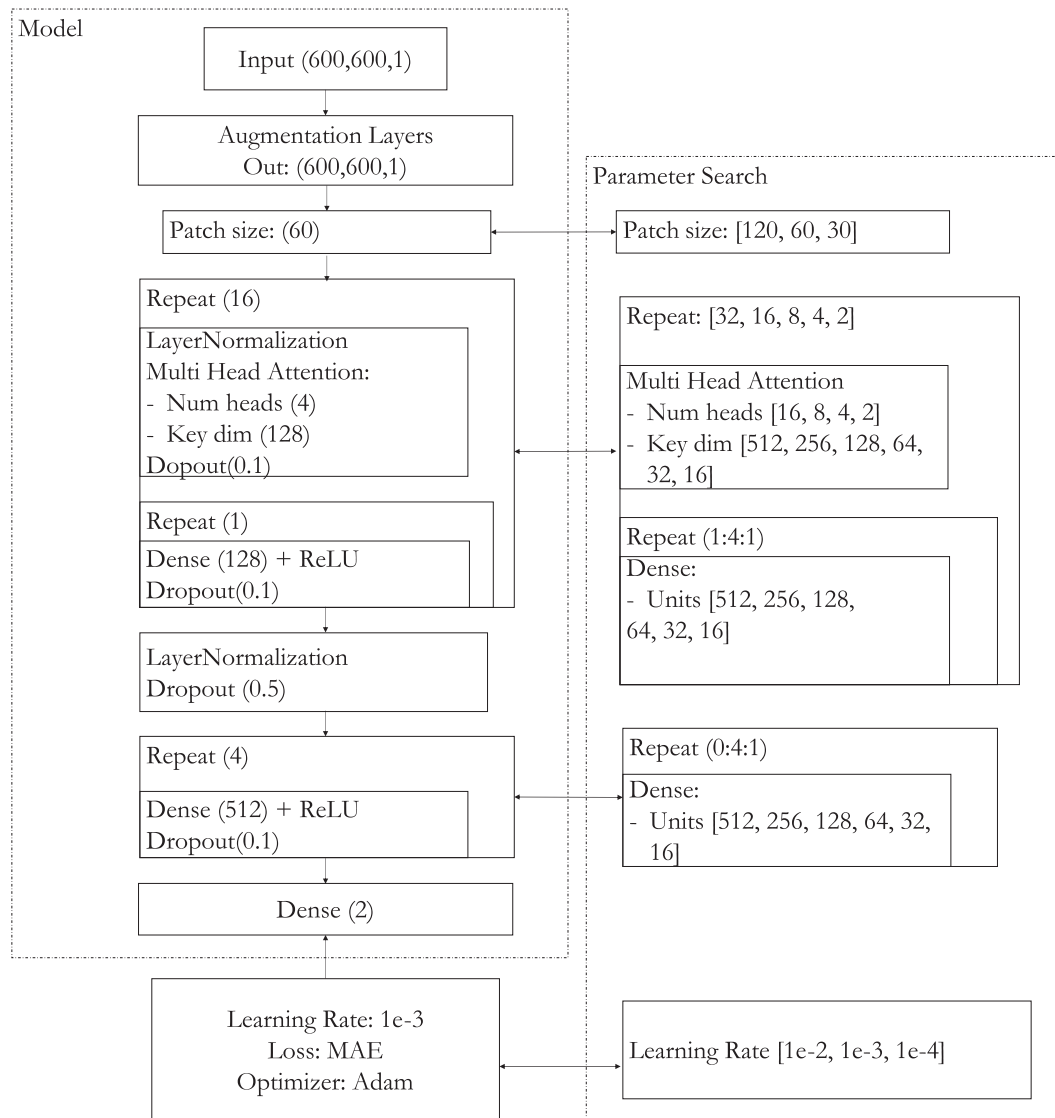


Fig. 4. The optimised architecture of the VisionTransformer-like model and chosen hyperparameters are on the left, and the searched hyperparameters are on the right. The syntax (Start:Stop:Stepsize) and [Option 1, Option 2, ...] is used.

to, e.g., randomized processes (such as the Hyperbandsearch, initialization of weights or randomized augmentation layers), floating point errors, enabled XLA (Accelerated Linear Algebra), or different numbers or types of GPUs. However, assuming the fixed conditions, the same dataset, and an unchanged arrangement of layers, the behavior of the networks presented can be expected to be reproducible.

2.7. Adapting attention mapping

Attention mapping is a common method for analysing predictions of CNNs that solve image classification tasks. One of the most established methods for this is Grad CAM (Gradient-weighted Class Activation Mapping) [33]. However, no established method exists for analysing predictions from images that solve regression tasks. Therefore, this method is adapted to evaluate the reliability of the predictions and show insights into the trained models' sensitivity regarding the modes' course. To modify this algorithm for a regression problem instead of a classification problem, specific changes must be made. In classification problems, labels are one-hot encoded, resulting in negative gradients typically being ignored because they do not activate the investigated class. However, in regression problems, negative gradients are just as important as positive gradients. Therefore, to calculate the attention

map, it is recommended to use the absolute values of both the last feature map and the gradient. However, investigations on the presented EfficientNet model have shown that the attention maps are dominated by artefacts resulting from the applied zero padding in the first layer and bias, cf. [34]. As a result, the attention maps presented here use the absolute gradient from the predicted values to the input as the attention map. The outcome is a colour-coded attention map, which is superimposed upon the original input image. Thus, the attention map shows which input image pixels are most likely to change the current predicted value. Note that the used colormap is min–max-normalized for each input individually.

3. Results and discussion

The training progress of both models is presented in Fig. 5. There is no indication of overfitting to the training data, as the validation error does not increase at the later epochs. Furthermore, the validation error is slightly lower than the training error since the dropout layers are applied during the training phase and are inactive during the validation phase. The data augmentation layer is active during training and validation but should not be active during testing/prediction. While a layer created using the TensorFlow-keras library can only differentiate

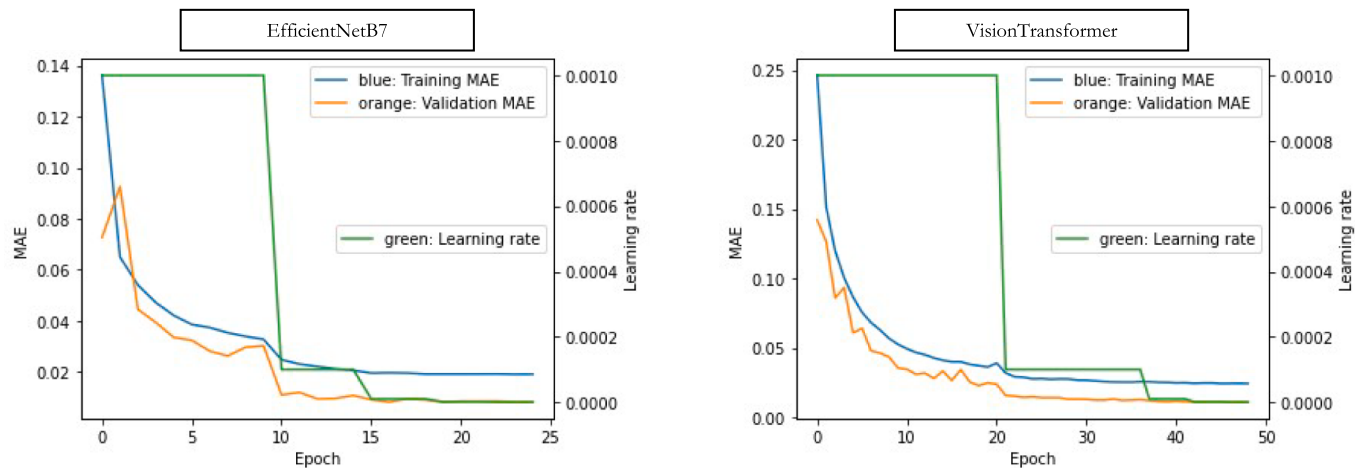


Fig. 5. The progress of the learning rate and the mean-absolute-error (MAE) for the training and validation dataset while training.

between training and validation status, deleting or skipping the pre-processing layers is necessary while predicting.

The EfficientNetB7 model, having much more but some pretrained weights from the ImageNet competition as starting values, converges faster than the Vision Transformer model with the randomly initialized weights. The rising error while training the first epoch of the EfficientNet model is due to the randomly initialized weights of the dense layer at the top of the pretrained convolutional weights. Training on four Quadro RTX 5000 graphic cards took approximately 24 min per epoch for the EfficientNetB7 model, while the Vision Transformer model took approximately 8 min per epoch. Determining the elastic values with the trained models using a CPU takes approximately 3 s for the EfficientNet and 0.3 s for the Vision Transformer per dispersion image. The Vision Transformer model is faster mainly because of its smaller number of weights, 12.3×10^6 , compared to 65.2×10^6 for EfficientNetB7.

3.1. Accuracy of the predictions

The mean absolute percentage error (MAPE) and R^2 for predicting the entire simulated test dataset with the final models is shown in Table 3, as

$$MAPE = \frac{1}{n} \sum_{i=1}^n |\text{percentage error}| = \frac{100}{n} \sum_{i=1}^n \left| \frac{\text{Label}_i - \text{Prediction}_i}{\text{Label}_i} \right| \quad (3)$$

and

$$R^2 \text{ (coefficient of determination)} = 1 - \frac{\sum_{i=1}^n (\text{Label}_i - \text{Prediction}_i)^2}{\sum_{i=1}^n (\text{Label}_i - \text{mean}(\text{Label}))^2} \quad (4)$$

where n is the number of samples within the dataset, the label is the value used within the simulation. Prediction_i represents the back-scaled output of the models, which involves reversing the min–max normalization process, see Eq. (2). These results, presented in Table 3, closely resemble the training and validation outcomes shown in Fig. 5, even though no data augmentation was applied.

Table 3

The predictions mean-absolute-percentage-error (MAPE) and R^2 regarding the simulated test dataset, E_{norm} and Poisson's ratio (ν).

Model's prediction on the simulated test dataset	MAPE for $E_{\text{norm}} [\%]$	MAPE for Poisson's ratio (ν) [%]	$R^2 E_{\text{norm}}$	R^2 Poisson's ratio (ν)
EfficientNet	2.94	0.82	0.9988	0.9976
Vision Transformer	2.13	1.16	0.9996	0.9932

Fig. 6 and Fig. 7 shows the error distribution for predicting the simulated test dataset. On the left for predicting E_{norm} , and on the right for predicting Poisson's ratio (ν). On the bottom is the percentage error, and on the top is the absolute difference between the label (actual value) and the predicted elastic constant. As expected, the error distribution is similar over the parameter range but slightly higher, close to the limits of the selected parameter range for the training dataset, as evidenced by Table 5. Consequently, the percentage error tends to rise for lower label values. The scatter plot at the bottom displays the absolute percentage errors. The colormap has been clipped to five percent for visibility and comparability reasons. Overall, predicting values near the limits of the trained value range is more error-prone, even when using perfect simulated data.

In standard publications, the performance of models is often tested using a single measurement example. Considering that a predicted value within the learned value range is expected for a completely arbitrary input since normalization techniques are included in the models and the performance varies over the learned value range, more diverse data is needed for testing NNs than other models. Therefore, besides the simulated dispersion images, the models are additionally tested on seven different material samples and variations of them, covering a wide range of the learned parameters, Table 4. Fig. 8 shows the variations within the measured dispersion images for the brass sheet measurement due to slightly different signal processing. These slight variations are applied to assess the stability of the model's predictions. Variations one and two (Var 1, Var 2) include only minor changes. Thus, we expect a prediction similar to that of the original input. Variant one (Var 1) is a slight dilation that widens the modes in the image, leading to more unsharp information. The second variation (Var 2) includes minor artifacts that appear due to suboptimal thresholding and omit the subsequent image optimization described in Section 2.3. Modification three (Var 3) is the image from modification two, including 20 % binary noise. This process is analogous to the application of noise within the data augmentation.

The percentage error (PE) of the model's predictions for the measurement dataset and its variations is shown in Table 4. The brackets contain the percentage error for the variations of the measured dispersion image (Var 1, Var 2, Var 3). It is visible that the models can perform slightly differently depending on variations of the same initial image. The field label quality indicates the trustworthiness of the assumed reference values (labels). Figure 10 shows the superimposed simulated (green) and measured dispersion images used to determine the label value for the elastic constants. The process of quantifying label quality is challenging due to the necessity of visually comparing lines to ascertain a match. Furthermore, real-world materials, which are assumed to be isotropic, may exhibit effects such as damping or directional dependencies, which are not accounted for in the simulated superimposed

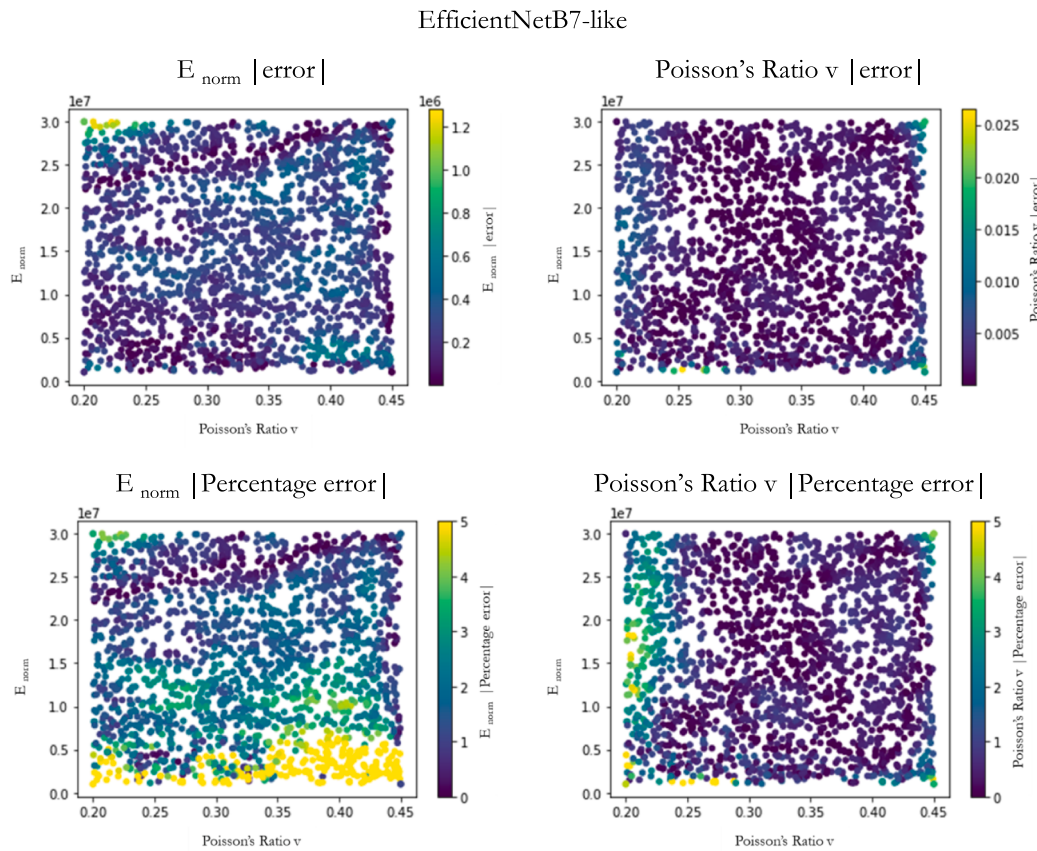


Fig. 6. Left E_{norm} and right side Poisson's ratio (v) prediction error of the simulated test dataset with the EfficientNetB7 based model. The x and y-axis show the labels, while the y-axis shows the selected elastic constant's actual error (top) and percentage error, including a clipped colormap to five percent (bottom).

data. Consequently, a minor error in the prediction does not necessarily indicate unsatisfactory results. Variation 3 (the added noise) does not significantly affect the prediction. This is as expected since noise was also included in the augmentation layers and, therefore, is well-known to the model. Indeed, there is an exception. On closer inspection of the EfficientNetB7 model predicting E_{norm} , it is shown that the introduction of additional noise impacts the results if certain regions within the dispersion images lack the expected modal information, see Table 4 and Fig. 9 Titanium sheet. However, the prediction of the EfficientNet-like model appeared to be unreliable for the dispersion image of the titanium sheet, probably due to the significant lack of information. In contrast, the Vision Transformer-like model appeared more robust to this measurement artifact.

Variations 1 and 2 result in only minor visible differences in the mode shape compared to the initial images, see Fig. 8. Therefore, the prediction is expected to be equal to the original input. The unexpected variation within the prediction accuracy, especially for the EfficientNet-like model, is noteworthy since the widening (dilation) of the mode shape and appearing artifacts are included in the augmentation layers. Therefore, it is concluded that the results of the VisionTransformer-like model are more reliable, as the predictions are more consistent regarding the variations compared to the EfficientNet-like model.

Generally, it can be assumed that the model's predictions are based on different characteristics since their architecture and the results in Table 4 are different. The EfficientNetB7 architecture utilizes convolutional layers mainly in the form of inverted residual blocks (MBConv blocks) and global average pooling, which might cause some difficulties. The EfficientNet-based model's performance is more affected by the variations within the mode shapes (Var 1, Var 2, Var 3) than the Vision Transformer model. This is due to the convolutional kernels' inherent ability to learn mainly from appearing gradients in images. Therefore,

the prediction of the EfficientNet-based model depends on highly specific appearing mode shapes and their relation to each other. The evidence supporting this assumption is that both models perform similarly on the perfect simulated test dataset, see Table 3, Fig. 6, and Fig. 7 but are slightly different on the measured dataset and its variations, Table 4. It might be assumed that the prediction using the EfficientNet-like model is entirely impartial to the position of the mode shape within the dispersion image as long as it exists somewhere. However, in the author's opinion, this is unlikely. Supporting this assumption is that the positional information is slightly shifted with respect to the kernel size while using convolutional layers. Additionally, the applied convolutional kernels do not have any information about their actual position while computing. However, the positional shift might be learned or transferred through the skip connection (residual blocks). However, the global average pooling layer at the end of the convolution layers deletes any positioning information for the extracted shapes. On the other hand, deeper convolutional layers focus on identifying and extracting specific shapes and finding spatial relations between them. Therefore, positional information may have been processed previously. In contrast, Vision-Transformer models seem likelier to take advantage of the positional information of the mode shapes since the initial image-like information is not changed or averaged before it is forced to reduce its dimensionality and is interconnected.

Therefore, it is assumed that convolutional layers and global average pooling may be less suitable for solving dispersion image-like problems where position information is essential compared to a Vision Transformer-like architecture.

3.2. Attention mapping

Five images from the test dataset were employed to generate the

Vision Transformer

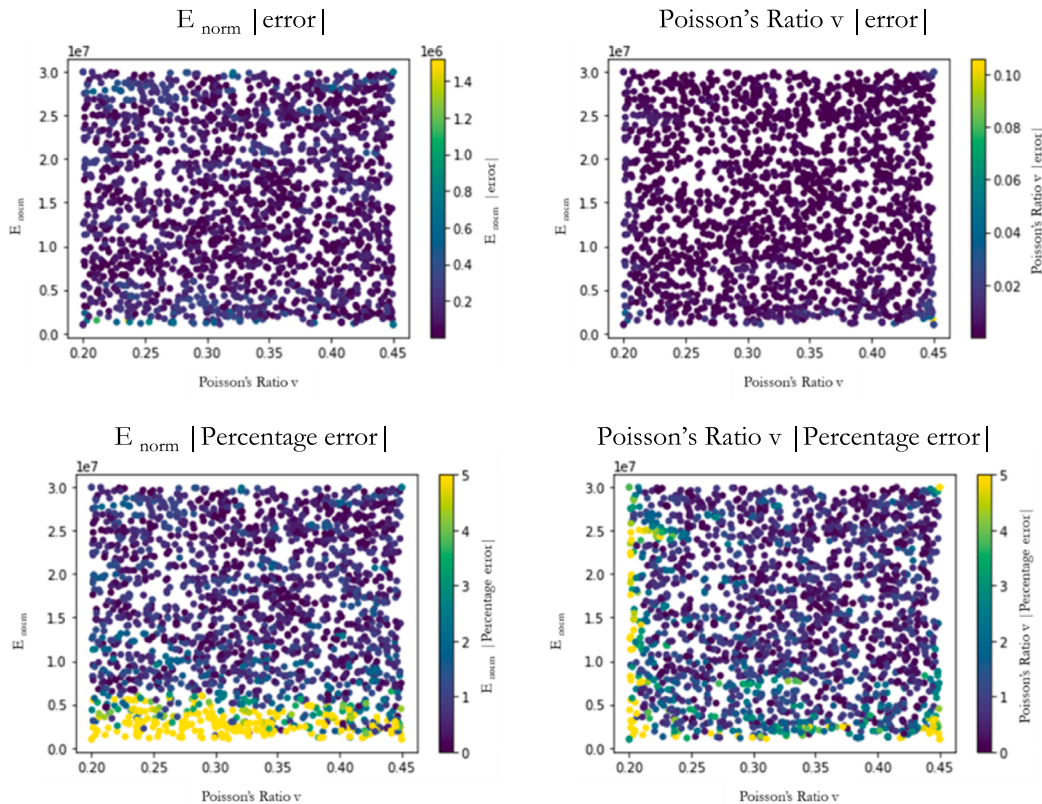


Fig. 7. Left E_{norm} and right side Poisson's ratio (v) prediction error of the simulated test dataset with the Vision Transformer based model. The x and y-axis show the labels, while the y-axis shows the selected elastic constant's actual error (top) and percentage error, including a clipped colormap to five percent (bottom).

Table 4

Percentage prediction errors (PE) across various measurement data samples and models. Variations of the input images are presented in brackets, original (Var 1 (dilation), Var 2 (thresholding), Var3 (noise)). Further details can be accessed via the supplementary materials file.

Model	EfficientNet		Vision Transformer		Assumed Labelquality
	PE for E_{norm} [%]	PE for Poisson's ratio (v) [%]	PE for E_{norm} [%]	PE for Poisson's ratio (v) [%]	
Overall	2 %	3 %	1 %	3 %	
Input / Material:	Original(Var 1, Var 2, Var 3)	Original(Var 1, Var 2, Var 3)	Original(Var 1, Var 2, Var 3)	Original(Var 1, Var 2, Var 3)	
Aluminium castAlMg4.5Mn	-6% (-8%, -9%, -4%)	0 % (3 %, 4 %, -1%)	-1% (-1%, -1%, -1%)	0 % (0 %, 0 %, 0 %)	good
AluminiumAl99.5	-1% (-2%, -3%, 0 %)	2 % (3 %, 3 %, 2 %)	1 % (0 %, 0 %, 0 %)	2 % (2 %, 3 %, 3 %)	good
Stainless steel1.4016	1 % (0 %, 1 %, -2%)	6 % (10 %, 12 %, 10 %)	-1% (-1%, -1%, -1%)	6 % (6 %, 6 %, 6 %)	good
Stainless steel1.4301	-4% (-4%, -6%, -5%)	1 % (5 %, 3 %, 0 %)	0 % (0 %, 1 %, 0 %)	-5% (-6%, -6%, -5%)	mid
Copper sheetCW008A	-2% (-3%, 1 %, 0 %)	0 % (1 %, 1 %, 0 %)	-2% (-2%, -2%, -2%)	1 % (0 %, 0 %, 0 %)	good
Brass sheetCuZn CW508L	-2% (-3%, -3%, -1%)	1 % (0 %, 0 %, 0 %)	-3% (-3%, -3%, -3%)	1 % (1 %, 1 %, 1 %)	good
Titanium sheetTi2 3.7035	-1% (-2%, -4%, -12 %)	-12 % (-5%, -5%, -3%)	1 % (0 %, -1%, 0 %)	-3% (-2%, -2%, -3%)	mid

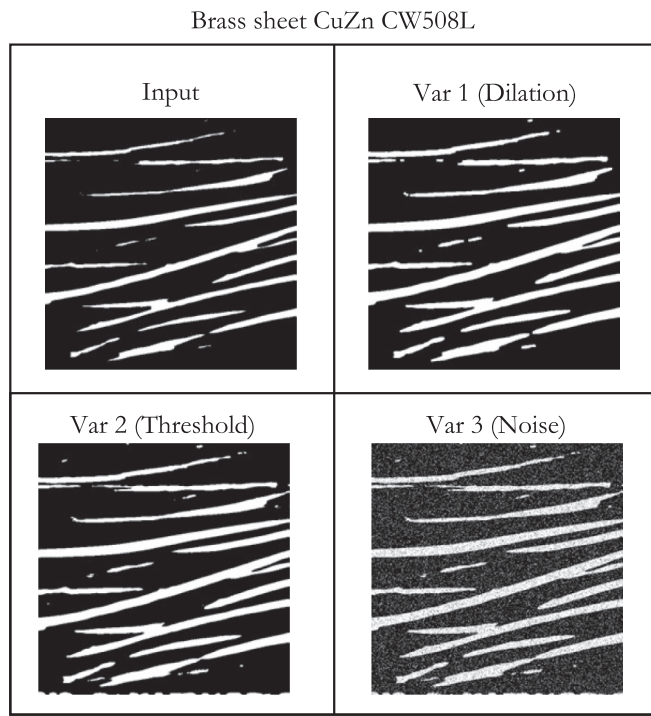


Fig. 8. Dispersion images resulting from the measurement of UGW propagation in the brass sheet. First, the initial dispersion image resulting from the measurement is shown. Second, variation 1 (Var 1) shows a slight dilation. Third, variation 2 (Var 2) contains some artifacts due to skipped preprocessing steps after thresholding. Finally, variation 3 (Var 3) shows uniformly distributed noise added to Var 2.

superimposed images, which are presented in Table 6 and Table 7. It is evident that the attention map per image regarding the different outputs appears similar. Consequently, the different output parameters share the extracted features from the input. The primary distinction between the two models is their response to empty areas in the dispersion image. This is due to the difference between convolutional layers, which can mainly learn from gradients in an image, and attention heads, which evaluate relations within an input. The dispersion images presented in Table 8, which show measurement data, exhibit broad mode curve shapes in the dispersion image due to imprecise measurements. Evidently, the EfficientNet-like model primarily responds to the gradients within the image. Furthermore, it is apparent that when a particular mode within a specific range is sensitive and has a wide mode curve shape, both the gradients approaching the mode from vacant areas and departing from the mode to vacant areas become sensitive. This indicates that the mean value, which may be considered to represent the assumed realistic course of the wide mode shape, may be used for the prediction.

The EfficientNet-like models' prediction is sensitive to modes that are present in the dispersion image. In contrast, the vision transformer model responds not only to existing modes but also to absent ones. The vision transformer model displays a clear correlation between high attention gradients in an empty area and the appearance of modes. This suggests that a shift in the current mode course in this specific area would have the most significant impact on the outcome. Additionally, the vision transformer appears to have access to a more comprehensive set of information from the same input as the EfficientNet-like model, as it is able to draw conclusions not only from gradients within the image but also from empty areas. Furthermore, with regard to the EfficientNet-like model, it can be seen that the S1 mode in the low wavenumber range is likely to change the current prediction in all cases presented, as similarly proposed by [2].

The measurement data and its variations, as shown in Table 8 and Table 9 indicate that the sensitive area changes within the same images

and their variations. This observation supports the hypothesis that predictions are based on various features appearing in the dispersion image. Additionally, compared to Table 6 and Table 7, adding noise allows the EfficientNet-like model to also make predictions from the now noisy, empty areas in the dispersion images. Furthermore, the EfficientNet-like model occasionally identifies a sensitive boundary area at the bottom, which is incorrect. Both models are affected by the vertical cut in the dispersion image of the titanium specimen. This vertical cut is an artefact that may be helpful to implement in future data augmentation, as it appears to be a consequence of insufficient resolution in the spatial domain.

These results support the hypothesis that the prediction is based on many different features, which are selected individually depending on the predicted parameters, the architecture and its weights, and the input data.

4. Conclusion

It is shown that CNN-like and Vision Transformers-like architectures can learn to precisely predict the isotropic elastic constants from measurement dispersion images in the frequency-wavenumber domain, representing ultrasonic guided wave propagation, even if only trained with simulated data. Therefore, dedicated data augmentation techniques are introduced to mimic real-world measurement data. It is shown that these methods can be implemented as layers within the model to cover artifacts occurring, like different widths of mode shapes, spectral leakage, noise, or other anomalies from the measurement within the simulated data.

Compared to regular inverse models, neural networks need more test data to ensure that the predictions are reliable and not arbitrary assumptions within the learned parameter range. 2 000 simulated dispersion images and seven measured dispersion images are used to test the reliability within the learned range and the ability of the models to predict measured data. The evaluation of the simulated dataset demonstrates that the percentage accuracy of the model's predictions depends on the value range. Different versions of the measured dispersion images are created to ensure the stability of the prediction for measurement data. The results suggest that the different models learned to solve the task differently while trained on the same data, most likely due to their different architectures. The EfficientNet-based model is assumed to focus on specific mode shapes and is sensitive to small changes in the dispersion images. In contrast, the Vision Transformer model appears to have learned globally connected features, making it less vulnerable to minor changes in the dispersion images. Although the overall accuracy of predicting the measurement dataset of the explored models, EfficientNet based model (2 % for E_{norm} and 3 % for Poisson's ratio (ν)), and the Vision Transformer based model (1 % for E_{norm} and 3 % for Poisson's ratio (ν)) is similar.

The presented approach is promising for automated applications because the elastic constants can be determined for a wide material parameter range without starting values, initial guesses, manual feature extraction, or prior knowledge of the measurement setup. Different measurement setups may produce various artifacts in the data, which should then be incorporated into the data augmentation process, as unknown artefacts may strongly affect the prediction. It is assumed that the method can be extended for anisotropic materials by using a procedure similar to the one described. In order to adapt the model for anisotropic, possibly layered materials, several changes are necessary. For instance, the number of output neurons needs to be adjusted based on the higher number of elastic constants for anisotropic materials. Due to the complex nature of these materials, such as having multiple layers with different orientations, the input data must also be modified. Combining dispersion images from multiple wave propagation directions may help provide enough input information to predict angle dependent elastic constants. Including additional input data, such as the thickness and number of layers or a reference system for the orientation

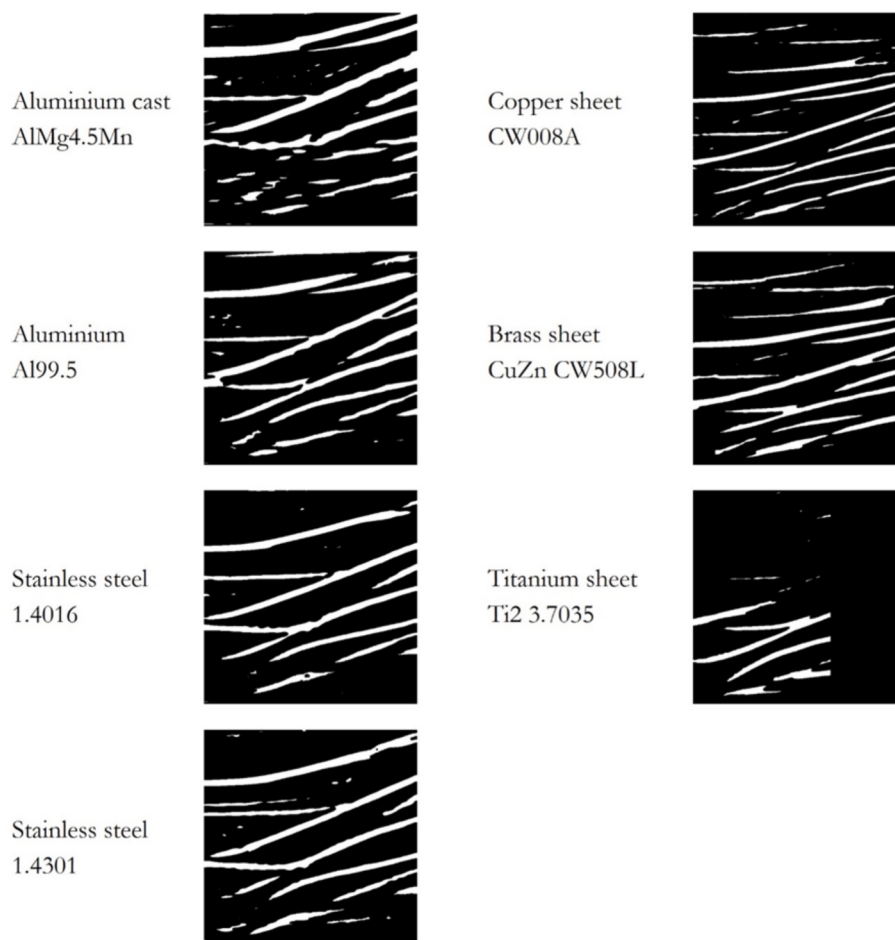


Fig. 9. Measured dispersion images used for the initial prediction in [Table 4](#).

of the dispersion images, could also be beneficial. Furthermore, a measurement setup capable of capturing a sufficient number of modes within the desired range is essential for identifying those modes sensitive to all elastic constants, as not all constants affect a specific mode. The main challenge is to create a dataset that sufficiently covers the desired range of anisotropic materials, as NNs hardly extrapolate.

In general, it is shown that neural networks can evaluate graph-like diagrams by treating them as images, which can be helpful in the case of unassignable curves or visualization/detection approaches in many research fields or applications, including guided wavefield data. Depending on the importance of the position information of the analyzed curves within the graph, it can be concluded that CNN-like architectures, including global average layers, are not preferable to Vision Transformers.

5. Author statement

During the preparation of this work the corresponding author used DeepL Write, Grammarly and ChatGPT to rephrase sentences and phrases for better understanding, clarity and spelling. After using this tool/service, the author(s) reviewed and edited the content as needed and take(s) full responsibility for the content of the publication.

CRediT authorship contribution statement

Mathias Held: Writing – original draft, Visualization, Validation, Software, Methodology, Investigation, Data curation, Conceptualization. **Jannis Bulling:** Writing – review & editing, Software. **Yevgeniya Lugovtsova:** Writing – review & editing, Validation, Supervision,

Software, Conceptualization. **Jens Prager:** Writing – review & editing, Supervision, Project administration, Funding acquisition, Conceptualization.

Declaration of competing interest

The authors declare the following financial interests/personal relationships which may be considered as potential competing interests: [Mathias Held reports financial support was provided by BAM Federal Institute for Materials Research and Testing. If there are other authors, they declare that they have no known competing financial interests or personal relationships that could have appeared to influence the work reported in this paper].

Data availability

Data will be made available on request.

Acknowledgements

The authors would like to thank the working group of Prof. Dr. Bernd Henning from the Chair of Electrical Measurement Technology (EMT) at the University of Paderborn for helpful discussions and for sharing their outstanding knowledge about material characterization with ultrasonic guided waves. The authors are also grateful for the funding and support provided by the Federal Institute for Materials Research and Testing (BAM), which made this research possible.

Appendix A. Supplementary material

Supplementary material to this article can be found online at <https://doi.org/10.1016/j.ultras.2024.107403>.

References

- [1] B. Hosten, M. Castaings, H. Tretout, H. Voillaume, Identification of composite materials elastic moduli from Lamb wave velocities measured with single sided, contactless ultrasonic method, AIP Conf. Proc. 557 (2001) 1023–1030.
- [2] J. Bulling, G. Franosch, Y. Lugovtsova, J. Prager, Sensitivity of ultrasonic guided waves to elastic constants: a numerical study, Eur. Workshop Struct. Health Monitor. (2021).
- [3] A.G. Every, W. Sachse, Determination of the elastic constants of anisotropic solids from acoustic-wave group-velocity measurements, Phys. Rev. B 42 (1990) 8196–8205.
- [4] S. Eros, J.R. Reitz, Elastic constants by the ultrasonic pulse echo method, J. Appl. Phys. 29 (1958) 683–686.
- [5] M.F. Markham, Measurement of the elastic constants of fibre composites by ultrasonics, Composites 1 (1970) 145–149.
- [6] M. Castaings, B. Hosten, T. Kundu, Inversion of ultrasonic, plane-wave transmission data in composite plates to infer viscoelastic material properties, NDT & E Int. 33 (2000) 377–392.
- [7] M. Kersmans, A. Martens, N. Lammens, K. Van Den Abeele, J. Degrieck, F. Zastavnik, L. Pyl, H. Sol, W. Van Paepengem, Identification of the elastic properties of isotropic and orthotropic thin-plate materials with the pulsed ultrasonic polar scan, Experiment. Mech. 54 (2014) 1121–1132.
- [8] D. Clorenne, C. Prada, D. Royer, Local and noncontact measurements of bulk acoustic wave velocities in thin isotropic plates and shells using zero group velocity Lamb modes, J. Appl. Phys. 101 (2007).
- [9] D. Clorenne, C. Prada, D. Royer, Laser ultrasonic inspection of plates using zero-group velocity lamb modes, IEEE Trans. Ultras., Ferroelect. Frequency Control 57 (2010) 1125–1132.
- [10] A.A. Eremin, E.V. Glushkov, N.V. Glushkova, R. Lammering, Evaluation of effective elastic properties of layered composite fiber-reinforced plastic plates by piezoelectrically induced guided waves and laser Doppler vibrometry, Composite Struct. 125 (2015) 449–458.
- [11] M. Webersen, S. Johannesmann, J. Düchting, L. Claes, B. Henning, Guided ultrasonic waves for determining effective orthotropic material parameters of continuous-fiber reinforced thermoplastic plates, Ultrasonics 84 (2018) 53–62.
- [12] P. Kudela, M. Radzinski, P. Fiborek, T. Wandowski, Elastic constants identification of fibre-reinforced composites by using guided wave dispersion curves and genetic algorithm for improved simulations, Composite Struct. 272 (2021) 114178.
- [13] M. Sale, P. Rizzo, A. Marzani, Semi-analytical formulation for the guided waves-based reconstruction of elastic moduli, Mech. Syst. Signal Proc. 25 (2011) 2241–2256.
- [14] S. Johannesmann, L. Claes, N. Feldmann, H. Zeipert, B. Henning, 'Lamb wave based approach to the determination of acoustic material parameters', *tm* -, Technisches Messen 89 (2022) 493–506.
- [15] M. Ryzy, I. Veres, T. Berer, M. Salfinger, S. Kreuzer, G. Yan, E. Scherleitner, C. Grünsteidl, Determining longitudinal and transverse elastic wave attenuation from zero-group-velocity Lamb waves in a pair of plates, J. Acoustical Soc. Am. 153 (2023) 2090.
- [16] A.H. Orta, J. De Boer, M. Kersemans, C. Vens, K. Van Den Abeele, Machine learning-based orthotropic stiffness identification using guided wavefield data, Measurement 214 (2023) 112854.
- [17] Y. Jing, C. Jian-Chun, A new inverse method of elastic constants for a fibre-reinforced composite plate from laser-based ultrasonic lamb waves, Chinese Phys. Lett. 18 (2001) 1620–1623.
- [18] Rautela, Mahindra, S. Gopalakrishnan, Karthik Gopalakrishnan, and Yiming Deng. 2020. "Ultrasonic Guided Waves Based Identification of Elastic Properties Using 1D-Convolutional Neural Networks." In *2020 IEEE International Conference on Prognostics and Health Management (ICPHM)*, 1–7.
- [19] K. Fukushima, Neocognitron: A self-organizing neural network model for a mechanism of pattern recognition unaffected by shift in position, Biolog. Cybernetics 36 (1980) 193–202.
- [20] M. Rautela, H. Armin, J. Senthilnath, S. Gopalakrishnan, Inverse characterization of composites using guided waves and convolutional neural networks with dual-branch feature fusion, Mech. Adv. Mater. Struct. (2021) 1–17.
- [21] H.J. Lim, H. Sohn, Online stress monitoring technique based on lamb-wave measurements and a convolutional neural network under static and dynamic loadings, Experiment. Mech. 60 (2020) 171–179.
- [22] Y. Lecun, L. Bottou, Y. Bengio, P. Haffner, Gradient-based learning applied to document recognition, Proc. IEEE 86 (1998) 2278–2324.
- [23] Shukla, Khemraj, Patricio Clark Di Leoni, James Blackshire, Daniel Sparkman, and George Em Karniadakis. 2020. "Physics-informed neural network for ultrasound non-destructive quantification of surface breaking cracks." In, arXiv:2005.03596.
- [24] K. Shukla, A.D. Jagtap, J.L. Blackshire, D. Sparkman, G. Em Karniadakis, A physics-informed neural network for quantifying the microstructural properties of polycrystalline nickel using ultrasound data: a promising approach for solving inverse problems, IEEE Signal Proc. Magazine 39 (2022) 68–77.
- [25] Stender, M. 2020. 'Data-Driven Techniques for the Nonlinear Dynamics of Mechanical Structures', Dissertation, TU Hamburg.
- [26] Song, Chongmin. 2018. "The scaled boundary finite element method : introduction to theory and implementation." In, 1 online resource. Hoboken, New Jersey: John Wiley & Sons.,
- [27] H. Gravenkamp, Efficient simulation of elastic guided waves interacting with notches, adhesive joints, delaminations and inclined edges in plate structures, Ultrasonics 82 (2018) 101–113.
- [28] Webersen, Manuel. 2021. 'Zerstörungsfreie Charakterisierung der elastischen Materialeigenschaften thermoplastischer Polymerwerkstoffe mittels Ultraschall', Veröffentlichungen der Universität.
- [29] Tan, Mingxing, and Quoc V. Le. 2019. "EfficientNet: Rethinking Model Scaling for Convolutional Neural Networks." In, arXiv:1905.11946.
- [30] Dosovitskiy, Alexey, Lucas Beyer, Alexander Kolesnikov, Dirk Weissenborn, Xiaohua Zhai, Thomas Unterthiner, Mostafa Dehghani, Matthias Minderer, Georg Heigold, Sylvain Gelly, Jakob Uszkoreit, and Neil Houlsby. 2020. "An Image is Worth 16x16 Words: Transformers for Image Recognition at Scale." In, arXiv: 2010.11929.
- [31] Meta-AI-Research. 2024. 'paperswithcode.com', Meta AI Research, Accessed 23.01. <https://paperswithcode.com/task/image-classification>.
- [32] L. Gai, M. Xing, W. Chen, Y.i. Zhang, Xu. Qiao, Comparing CNN-based and transformer-based models for identifying lung cancer: which is more effective? Multimedia Tools Appl. (2023).
- [33] Selvaraju, Ramprasaath R., Michael Cogswell, Abhishek Das, Ramakrishna Vedantam, Devi Parikh, and Dhruv Batra. 2016. "Grad-CAM: Visual Explanations from Deep Networks via Gradient-based Localization." In, arXiv:1610.02391.
- [34] Alsallakh, Bilal, Narine Kokhlikyan, Vivek Miglani, Jun Yuan, and Orion Reblitz-Richardson. 2021. "Mind the Pad - CNNs can Develop Blind Spots." In, arXiv: 2010.02178. 9th International Conference on Learning Representations, {ICLR} 2021, Virtual Event, Austria, May 3–7, 2021: OpenReview.net.